Determination of fracture strength and fracture energy of (metallo-) ceramics by a wedge loading methodology and corresponding cohesive zone-based finite element analysis

Farle, Ann Sophie; Krishnasamy, Jayaprakash; Turteltaub, Sergio; Kwakernaak, Cees; van der Zwaag, Sybrand; Sloof, Willem G.

DOI
10.1016/j.engfracmech.2018.03.014

Publication date
2018

Document Version
Final published version

Published in
Engineering Fracture Mechanics

Citation (APA)
Farle, A. S., Krishnasamy, J., Turteltaub, S., Kwakernaak, C., van der Zwaag, S., & Sloof, W. G. (2018). Determination of fracture strength and fracture energy of (metallo-) ceramics by a wedge loading methodology and corresponding cohesive zone-based finite element analysis. *Engineering Fracture Mechanics*, *196*, 56-70. https://doi.org/10.1016/j.engfracmech.2018.03.014

Engineering Fracture Mechanics 196 (2018) 56–70

Contents lists available at ScienceDirect

Engineering Fracture Mechanics

journal homepage: www.elsevier.com/locate/engfracmech

Determination of fracture strength and fracture energy of (metallo-) ceramics by a wedge loading methodology and corresponding cohesive zone-based finite element analysis

Ann-Sophie Farle[a], Jayaprakash Krishnasamy[b], Sergio Turteltaub[b], Cees Kwakernaak[a], Sybrand van der Zwaag[b], Willem G. Sloof[a,*]

[a] Department of Materials Science and Engineering, Delft University of Technology, Mekelweg 2, 2628CD Delft, The Netherlands
[b] Faculty of Aerospace Engineering, Delft University of Technology, Kluyerweg 1, 2629HS Delft, The Netherlands

ARTICLE INFO

Keywords:
Fracture strength
Fracture energy
Cohesive-zone modelling
Ceramics
Acoustic emission
Self-healing

ABSTRACT

A wedge loaded testing methodology to determine the fracture energy and strength of (semi-) brittle (metallo-)ceramics is presented. The methodology combines a tailored specimen geometry and a comprehensive finite element analysis based on cohesive zone modelling. The use of a simulation-based approach to extract both fracture strength and energy from experimental data avoids the inherent inaccuracies found in closed-form expressions that rely on a priori assumptions about the deformation field. Results from wedge splitting tests on Ti_3SiC_2 and Ti_2AlC (MAX phase) materials are used to illustrate the procedure. The simulation-based approach is further validated by comparing the fracture strength and fracture energies predicted by the proposed method and those indicated by a conventional four-point bending fracture toughness test (ASTM standard). The new protocol offers the possibility to measure not only the fracture properties of brittle material in its pristine state but also in the healed state.

1. Introduction

Testing procedures to accurately quantify the fracture strength and fracture energy of materials typically depend on a variety of factors such as the material's elastic characteristics (compliant or stiff) and its fracture response (ductile or brittle). The absolute values may also depend on loading rates, the measured primary response variables such as loads and displacements and the post-processing of the recorded data. Ease of sample preparation, insensitivity to non-defined parameters and repeatability of the results also plays a significant role in the design of a testing procedure.

For brittle materials, it is also known that the measured fracture properties depend on the ratio between the size of the critical flaw(s) and the zone where the stress concentrates in the sample (e.g., the measured fracture strength in a tensile test would typically be different from that in a bending test). Bending tests have been accepted as the simplest yet least precise test method to determine fracture strength and fracture energy of brittle materials [1,2]. Bending tests commonly require controlled pre-cracks, which are difficult to produce and measure in most (semi-) brittle materials [2,3]. Moreover, this test, assuming a machining induced pre-crack in the material, may overestimate the fracture toughness and is highly sensitive to machining induced surface imperfections [3]. The sensitivity to surface flaws furthermore creates the necessity for higher sampling sizes to compensate for measurement error. The wedge splitting test was established by Tschegg [4]. Wedge-loading to determine fracture properties in concrete and concrete like

* Corresponding author.
E-mail addresses: annsophiefarle@hotmail.com (A.-S. Farle), W.G.Sloof@tudelft.nl (W.G. Sloof).

https://doi.org/10.1016/j.engfracmech.2018.03.014
Received 23 November 2016; Received in revised form 11 February 2018; Accepted 13 March 2018
Available online 12 April 2018
0013-7944/

Nomenclature

(X)FEM	(eXtended) Finite element analysis
CZM	Cohesive Zone Modelling
Δ	Effective cohesive opening displacement
E	Young's modulus
EDM	Electric discharge machining
f	Coefficient of kinematic friction
G_c	Fracture energy
K	Cohesive stiffness
K_{1C}	Stress intensity factor in mode I
LEFM	Linear Elastic Fracture Mechanics
l_{fpz}	Cohesive zone length
MAX	$M_{n+1}AX_n$
SCB	Semi-circular bend test
T	Effective traction
ν	Poisson's ratio
WLS	Wedge loaded specimen
σ_c	Critical traction & effective fracture strength

materials has been performed by Bruhwiler et al. [5] but not yet modified and applied to the specific requirements of ceramic materials. In addition to the aforementioned difficulties, the quantification of crack-healing efficiency in self-healing materials requires methods to create stable cracks. Chevron-notched specimens can negate problems caused by pre-cracking attempts so in this sense this sample geometry is generally viewed as an improvement compared to samples without chevrons [2]. Furthermore, when setting the requirements for an optimally informative test method, it is clear that an ideal test should not only report the load-displacement data but also the actual crack length at every stage of the cracking process. For the determination of the crack length both optical [6] and acoustical methods [7] are available while in specific cases also X-ray tomographic methods [8] can be used.

Aside from the physical testing requirements defined above, an important aspect of a testing methodology is the interpretation of the measured data. The quantities of interest, fracture strength and fracture (propagation) energy, are typically not measured directly but rather need to be derived from the measured response variables such as loads and actual crack dimensions. For fracture properties, the traditional approach has relied on using the theory of Linear Elastic Fracture Mechanics (LEFM), which, often in combination with analytical solutions for simple geometries or finite element simulations (FEM) for complex geometries, is used to derive closed-form expressions from which the fracture strength and/or the fracture toughness can be computed (i.e., a critical value of the stress intensity fracture at which a crack propagates) [9,10]. An alternative approach is to conduct finite element (FEM) numerical simulations of the fracture test using a Cohesive Zone Modelling (CZM) approach [11,12]. In combination with the experimental data, the simulations can be used to extract the fracture properties of the material taking into account the whole fracture process, namely nucleation and propagation of a crack. CZM combines ingredients found in stress-based and energy-based formulations for fracture mechanics. CZM has been implemented in conjunction with cohesive elements and, more recently, within the so-called eXtended Finite Element Method (XFEM). This methodology overcomes some intrinsic limitations of the (traditional) LEFM approach since it can model both nucleation and propagation of cracks. CZM, with either cohesive elements or XFEM, has been applied, for example, in [13] to predict the fracture behaviour of adhesive joints, in [14] for the analysis of delamination in fiber-reinforced polymer (FRP) beams, in [15] to simulate the crack propagation in wood, in [16] to predict the fatigue crack nucleation and propagation in quasi-brittle materials, in [17] to estimate the fracture toughness of free standing 8 wt.% Y_2O_3-ZrO_2 (8YSZ) coatings and in [18] to analyze a specimen geometry to enhance crack stability for brittle materials and to improve closed-form formulas by deriving the so-called geometrical factor for different specimen dimensions. Other relevant work includes [19], where simulations

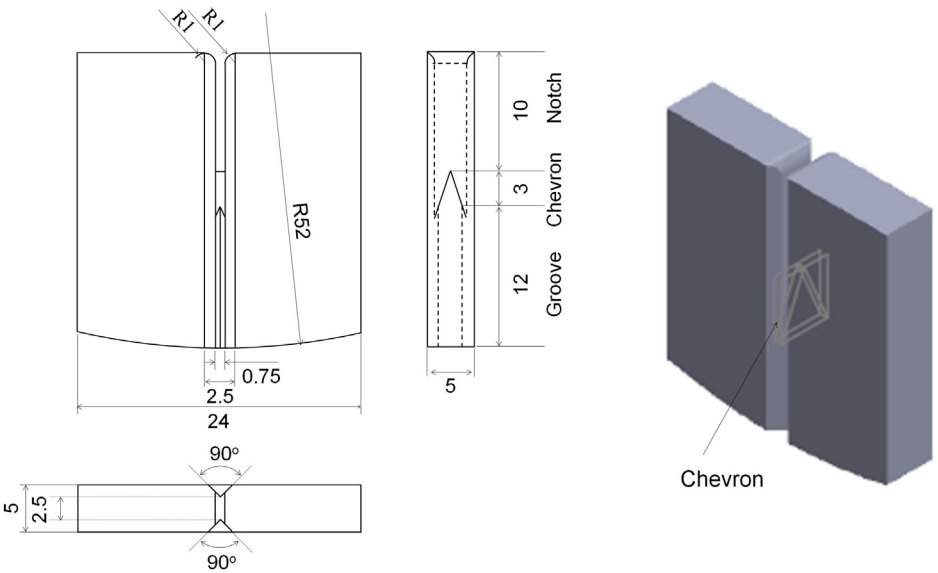

Fig. 1. Wedge splitting test specimen geometry with lengths in mm.

were conducted to predict the fracture properties of asphalt using a semi-circular bend test (SCB), and [20] where simulations were used to demonstrate the variability and anisotropy of fracture toughness of cortical bone tissue using the load-displacement curve obtained from the three-point bending tests.

While the accurate determination of the fracture properties of pristine (brittle) materials is demanding as it is, with the recent development of self-healing ceramic materials, a new requirement also has to be taken into account, namely that the sample is not split into separate pieces in the determination of the fracture strength and the fracture energy. Only if the crack is contained within the sample, the sample can be exposed to a simple (thermal) healing treatment not requiring uncontrolled manual realignment and clamping of the two fracture surfaces. The test set-up as described here, meets this important requirement.

So the aim of the work is to develop a fracture test method and data analysis protocol to determine both the fracture strength and the fracture toughness of a pristine brittle material in such a manner that after initial fracture testing the sample is in a state suitable for subsequent thermal healing and determination of the fracture properties of the healed sample. The current approach is demonstrated for two semi-brittle MAX phase ceramics, which not only have attractive mechanical properties at ambient and high temperatures [21] but also recover their mechanical strength upon high temperature annealing [8,22,23]. In the present analysis we only focus on the determination of the fracture properties in the pristine state. The determination of the fracture properties of these materials in a healed state is subject of a separate publication.

2. Experimental and modelling

2.1. Specimen design

The new chevron-notched, wedge-loaded specimen geometry (WLS) is shown in Fig. 1. The basal half-length is chosen as 0.48 times the longest height of the sample. A curvature with a radius of 52 mm as the base allows sample self-alignment under loading conditions. A chevron notch tip is located at a depth of 10 mm. The contact edges of the notch opening are rounded with a radius of 1 mm to minimize the friction with the loading-wedge.

A 90° guide-groove is machined into the side of the sample to reduce the thickness by half. The recommended thickness of 5 mm is within the limits set by the ASTM E647 standard for compact tension specimen [24]. In this study, samples with a basal half-length of 12 mm, a height of 25 mm and thickness of 5 mm were used.

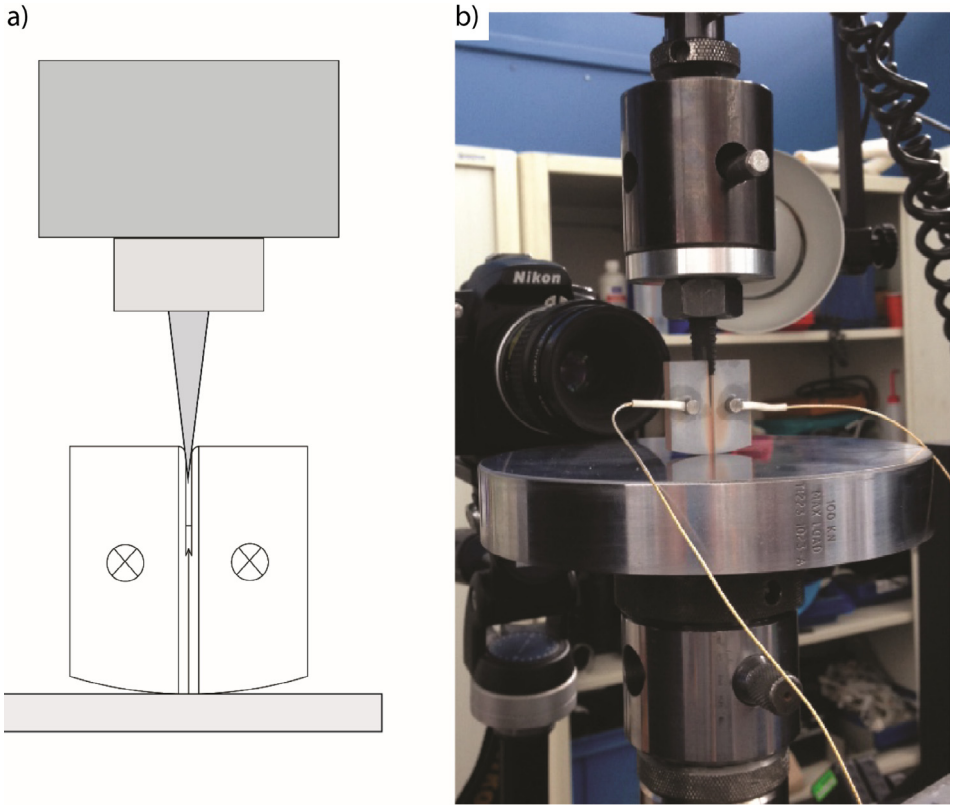

Fig. 2. Test setup of chevron-notched, wedge-loaded specimen (WLS) with microphone positions indicated (a) schematic and (b) actual test setup.

2.2. Samples and test setup

Samples of Ti_2AlC and Ti_3SiC_2 were synthesised by reactive sintering in a spark plasma sintering (SPS) furnace (HP D 25 SD, FCT Systeme GmbH, Germany). Ti_3SiC_2 starting powders of Ti (100 μm, > 99.5%, TLS Technik GmbH &Co., Germany), Si (45 μm, > 99.99%, TLS Technik GmbH &Co., Germany) and TiC (< 10 μm, 99%, ChemPur, Germany) were mixed for 4 h using a Turbula T2C Mixer (Willy A. Bachofer, Switzerland) with 5 mm alumina balls. Powder mixtures with molar ratios of Ti : Si : TiC with Ti and Si as 1 and varying TiC, viz.: 1.4 and 1.5, were sintered at 1500 °C for 4 h in 40 mm graphite moulds under a uniaxial pressure of 50 MPa. Similarly, Ti_2AlC was sintered from Ti, Al and graphite (> 99.5, 6 μm, Graphit Kropfmühl AG, Germany) in a ratio of 0.85: 1.05: 1.15 at 1400 °C for 30 min. The phase purity of the samples was determined via X-ray diffraction using a Bruker D8 ADVANCE diffractometer (Bruker, Germany) in the Bragg-Brentano geometry with a graphite monochromator and Co Kα radiation. The recorded X-ray diffractograms were processed with Bruker software DIFFRAC.EVA 4.1 software. Elastic properties were determined by Vickers indentation using a hardness tester (Zwick/Z2.5, Germany). Indents were created by loading the indenter with 5 N/s up to 50 N, holding for 12 s and unloading with 3.7 N/s. The density of the material was measured with the Archimedes method using an

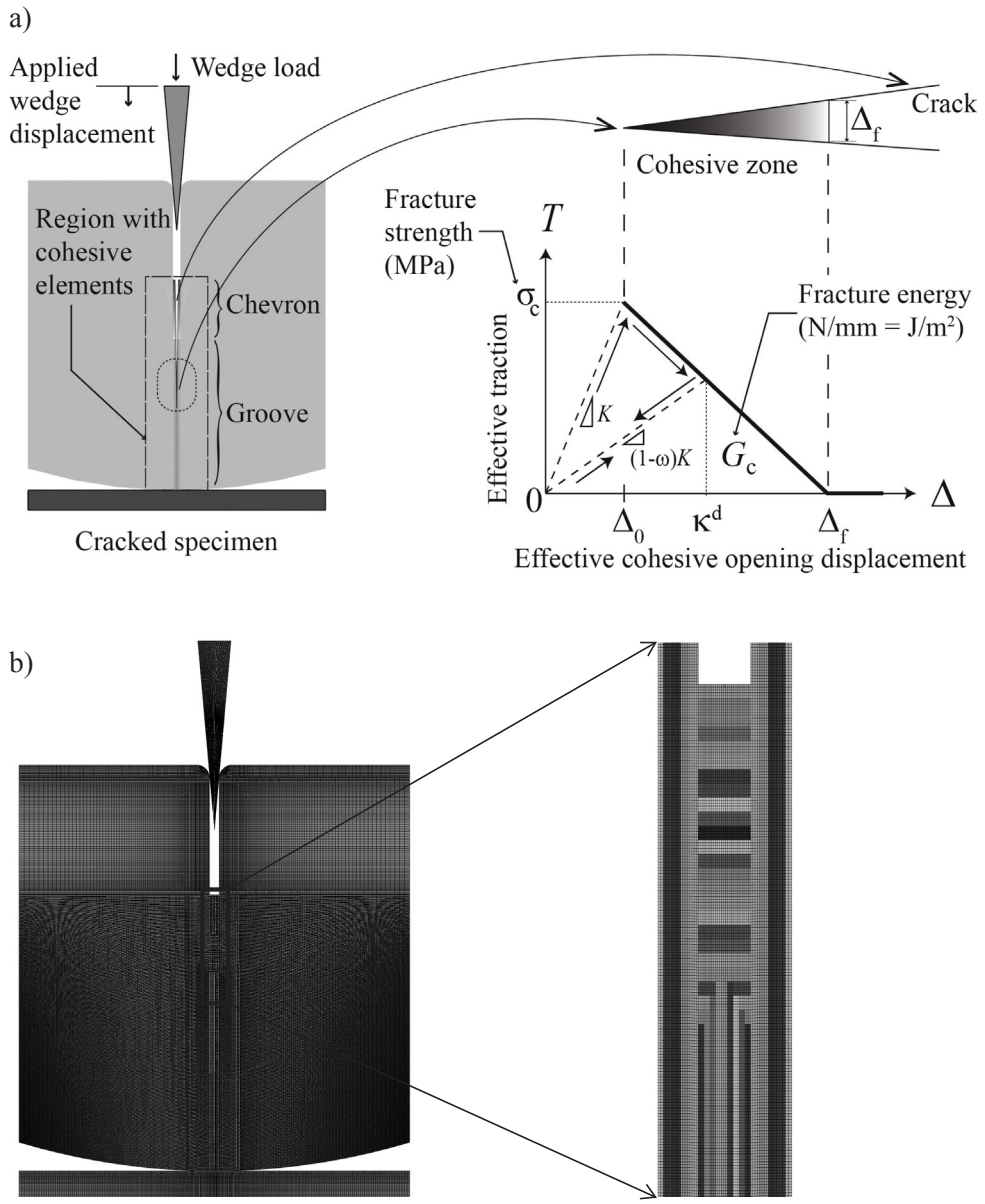

Fig. 3. . (a) Numerical model of wedge splitting test specimen with a bilinear cohesive relation implemented in cohesive elements to simulate the fracture process during testing. The area under the curve corresponds to the fracture energy per unit area required to fully separate the cohesive surface. (b) Finite element mesh of wedge splitting test specimen. The inset shows the elements in the chevron modelled with varying thicknesses.

analytical balance (Mettler Toledo AG-204, Switzerland) according to ASTM B 962 [25]. All Ti_2AlC and Ti_3SiC_2 samples were more than 92% dense.

All machining was carried out by electric discharge machining (EDM) with wire diameters of 0.25 and 0.1 mm.

The test setup is shown schematically in Fig. 2. Tests were performed using a 100 kN electro-mechanical load frame (Series 5500R, Instron, USA) that was fitted with a 10 kN load cell to suit the recorded load levels. The sample was placed on a flat stainless steel base-plate without further clamping. The quenched and tempered steel 10° wedge was lowered into the sample grove until it reached a pre-load of approximately 10 N.

Tests were carried out under closed-loop displacement control, with a fixed crosshead displacement rate of 0.01 or 0.1 mm/s. Crosshead displacement signal was calibrated by compression tests with strain gauge control to correct for rig deformation under the applied loads. The crosshead motion was stopped when a load drop of 50% from peak load was recorded. Upon termination, the crosshead motion was reversed leading to retraction of the wedge. Unloading curves were not recorded.

The recording of the acoustic events during the fracturing was performed with a Physical Acoustics module (PCI-2, 2 channel 40 MHz 18bit data-acquisition combined with ILS40 pre-amplifiers). Registration and post-processing were executed with the Physical Acoustics AEWin 1.70 (2005) software module. Prior to testing, two microphones were attached with paraffin wax to the right and left of the sample groove to allow registration of acoustic emission signals during the experiments. The sampling rate employed was 2 MHz with a 20 dB amplification factor. An acoustic event was recorded if the signal level of any microphone exceeded 5 mV. Every event was separately recorded as a waveform file containing 2048 points at 0.5 μs intervals. The energies recorded varied in a wide range between 1 aJ to 1 nJ. A cumulative energy as a function of time, termed the “acoustic energy”, was obtained through post-processing of the acoustic events. Here, the total acoustic energy is assumed to be proportional to the total amount of fracture introduced in the specimen. Final crack lengths and microstructure were determined by optical microscopy using a digital microscope (Keyence VHX-100, Osaka, Japan) and scanning electron microscopy (SEM), type JSM 6500F (JEOL Ltd., Tokyo, Japan) equipped with an energy dispersive spectrometer (EDS, type: ThermoFisher UltraDry 30 mm^2 detector) for X-ray micro-analysis (XMA) and with Noran System Seven software package for data acquisition and analysis. Surfaces and cross-sections, prepared by cutting with a diamond wafering blade, were ground using SiC paper up to 4000 grit and polished with diamond suspension up to 1 μm.

2.3. FEM with cohesive zone modelling

The extraction of fracture material properties is based on simulating the actual experimental set up using a Finite Element approach with cohesive zone modelling. Simulations are carried out using the commercial FEA package Abaqus (version 6.14). The finite element model of the chevron-notched, wedge-loaded specimen (WLS) test set up is shown in Fig. 3. For computational efficiency, the specimen is modelled as a two-dimensional domain under plane stress assumption. To simulate the three-dimensional features of the specimen, the chevron notch and the groove in the specimen geometry are modelled using a variable thickness. The fracture process is simulated using cohesive crack model, which describes fracture as a gradual process of formation of new surfaces. It replaces the classical singular fields at the crack tip with a process zone (i.e., the cohesive zone). The behaviour in the cohesive zone is described by a cohesive constitutive relation that relates the traction on the crack surface to the crack opening displacement. Within the finite element framework, the cohesive relation was implemented using zero-thickness cohesive elements. These elements were inserted along the inter-element boundaries to capture the onset and evolution of the fracture process (see, e.g., [26,27] for more details). In the present analysis, cohesive elements are inserted at the interfaces of all bulk elements in the regions where crack (s) are expected to initiate and propagate, in particular at the chevron and groove. A bilinear traction-separation relation [12] with linear softening is used to describe the local nucleation and crack-opening process within the numerical sample as shown in Fig. 3a and the corresponding finite element mesh is shown in Fig. 3b. The effect of the shape of the cohesive law on the overall response of the specimen is normally negligible [28–30], although in some cases it may affect the onset of unstable crack growth [31]. In the present quasi-static case a linear softening relation is sufficient. The critical traction σ_c corresponds the maximum effective traction value that can be transmitted through the cohesive surface (fracture strength) and the area under the curve corresponds to the fracture energy G_c required to fully separate the cohesive surface at a given location (i.e., per unit newly cracked area). The initial response of the cohesive surface before fracture is characterized by a cohesive stiffness K whose value is chosen as large as possible to avoid artificial compliance but still preventing a (numerically) singular response. After reaching the fracture strength, the progressive degradation of the load-carrying capacity of the cohesive zone is captured by a linear softening relation until the load is zero, which is interpreted as a fully-formed crack where no load can be transmitted for subsequent increases in the cohesive opening displacement. The effective cohesive opening displacement Δ and the effective traction T combine contributions from components that are normal and tangential to the cohesive surface. The cohesive relation is applicable for pure mode I (normal), pure mode II (tangential) or mixed-mode openings depending on the deformation at a given location (see, e.g., [32,24] for details).

A fine mesh is used in the region of interest (groove and chevron) and a coarser mesh is used in other regions. The mesh in the region of interest is chosen in accordance to the cohesive zone length l_{fpz}, which is defined here as

$$l_{fpz} = EG_c/\sigma_c^2 \tag{1}$$

where E is taken as the Young’s modulus of the material. The l_{fpz} refers to fracture process zone length (cohesive zone length) which is the region where a crack cohesive crack appears and eventually becomes a fully-separated surface (i.e., a crack in the classical sense) [11,33]. It can also be used as a measure of the brittleness of a material. Lower values of lfpz correspond to higher brittleness and vice

versa. The characteristic element size is chosen such that the cohesive zone can be accurately resolved, i.e., the cohesive zone spreads among several cohesive elements. The boundary conditions in the simulations are chosen such that they closely reproduce the testing conditions. The displacement of the top of the wedge is prescribed as a function of time according to the loading rate whereas the bottom of the support plate is modelled as simply-supported. The wedge and the support are included in the simulation as deformable parts. The contact between the wedge and the specimen is modelled as (Coulomb) dry-friction with a surface-based penalty (isotropic) formulation with a coefficient of kinematic friction f. The elastic responses of the wedge and the specimen are modelled using isotropic and linear relations with Young's modulus and Poisson's ratio taken as $E_w = 200$ GPa, $\nu_w = 0.3$ and, for the specimens, as follows:

Specimen	E_s	ν_s
Ti_3SiC_2	320 GPa	0.2
Ti_2AlC	260 GPa	0.18

where the subscript refers to the wedge (w) or specimen (s). The elastic properties of the specimens are obtained from published data [34–36] and verified with indentation tests whereas the wedge properties are taken from the wedge material's specification. The support is modelled as an elastic material that approximates a rigid body with frictionless contact used at the interface of the support and the specimen. Preliminary simulations including plasticity in both the specimen and the wedge were carried out to determine its likelihood of occurrence and its possible effect on the results. It was concluded that plastic behaviour is confined to a small region close to the cracks and its effect cannot be separated from the cohesive relation (i.e., at the length scale of the simulation, it is possible to model the bulk response of the material as elastic and use a cohesive relation to capture the inelastic behaviour).

Since the purpose of the simulations is to determine the fracture properties of the specimen, a parametric analysis was carried out varying the effective fracture strength σ_c and the effective fracture energy G_c. In addition, it is known that for a wedge-splitting test, friction can play a significant role [3]. Consequently, distinct values of the (kinematic) friction coefficient f used in Coulomb's model were considered.

2.4. Simulation setup

To simulate the test, a downward displacement of the top of the wedge is specified. Upon contact with the specimen, the specimen undergoes a loading dominated by an opening mode (mode I), although the actual loads at the crack tip are obtained from the simulation. The corresponding reaction force at the top of the wedge, which is obtained as a result of the simulation, is recorded throughout the simulation.

The procedure to extract the fracture material properties is as follows:

1. A preliminary elastic simulation is carried out for different values of the coefficient of friction. The value of f for which the *initial slope* of the simulation coincides with the initial slope of the experimental data to within a desired tolerance is then used for subsequent steps. If the experimental and the simulation responses deviate from a linear curve, then it is recommended to match the average slope until the onset of cracking as measured from the acoustic emission.

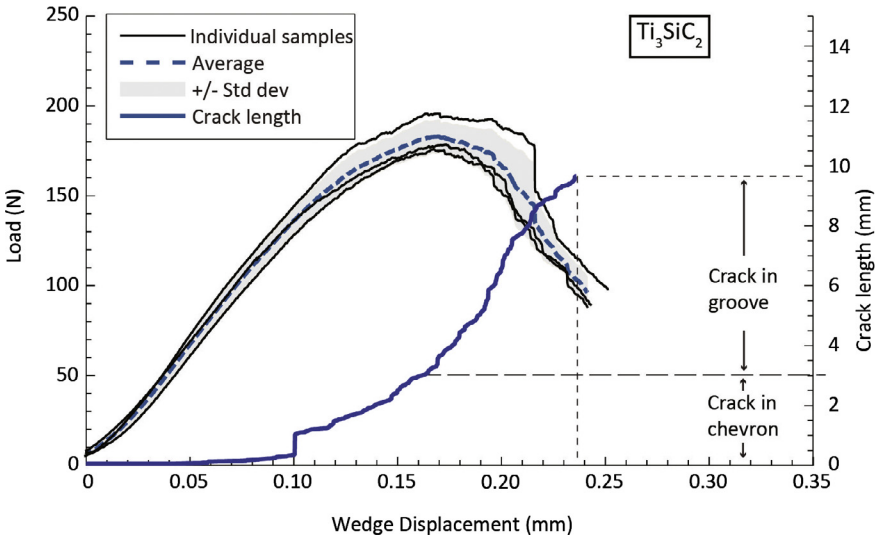

Fig. 4a. Wedge load (left axis) and normalized crack length (right axis) versus wedge displacement for Ti_3SiC_2 samples. The crack length is deduced from the acoustic energy and it is normalized using a directly measured crack length, namely 9.6 mm, at the end of the test.

2. With a chosen (fixed) coefficient of friction, a parametric analysis including fracture is carried out for different values of the fracture strength and fracture energy.
3. For each pair of values of fracture strength and energy, the wedge load is obtained as a function of the wedge displacement. This prediction is compared with the experimental response. The actual fracture material properties are taken as those for which the simulation provides the best approximation to the experimental data. In accordance with the CZM approach, the best fit is obtained by comparing the predicted and the experimentally-obtained maximum load and total energy dissipated. As a verification step, the crack length predicted in the simulation is also recorded as a function of the wedge displacement and compared with the experimental data.

3. Results and discussion

3.1. Experimental results

XRD analysis of the Ti_3SiC_2 samples revealed only minor amounts (< 5 wt.%) of TiC as a second phase in all samples. The variance in precursor ratios had no effect on the final composition; an effect not fully understood at this point, but beyond the scope/aim of this paper. According to XRD results spark plasma sintering of elemental powders resulted in pure Ti_2AlC samples. Ti_3SiC_2 samples consists of slightly elongated grains with a length between 20 and 80 μm. Ti_2AlC specimen have a similar morphology with grains of 50 μm (± 20 μm) maximum length and a width of max. 25 μm.

The measured wedge load as a function of the wedge displacement for the samples tested is shown in Fig. 4a for Ti_3SiC_2 and in Fig. 4b for Ti_2AlC.

Figs. 4a and 4b also show the measured crack length and cumulative acoustic signal as a function of the wedge displacement for one representative Ti_3SiC_2 sample and one Ti_2AlC sample. The crack growth curve for the Ti_3SiC_2 sample shows a slow and controlled crack propagation. For the Ti_2AlC sample, the crack growth is mostly controlled except during the transition from the chevron to the groove where the crack length increased abruptly. However, subsequent crack growth in the groove proceeded in a controlled fashion. In general the following regions of crack growth can be identified:

1. Slow propagation that occurs in the chevron due to the gradual increase in thickness of the specimen.
2. Fast propagation observed in the transition region between the chevron and the groove due to the sudden decrease in the thickness.
3. Subsequent slow propagation in the groove when the crack growth stabilizes because of the constant thickness in the groove.

Based on preliminary tests where the loading was interrupted at fixed intervals and the crack length was optically measured (not reported here for conciseness), a reasonably good correlation is found between crack propagation and acoustic energy, which indicates that this parameter can be used to estimate crack length. The use of acoustic emission data to measure onset of crack growth in fatigue testing is further described by Bassim et al. [37], Moorthy et al. [38] and Roberts et al. [39].

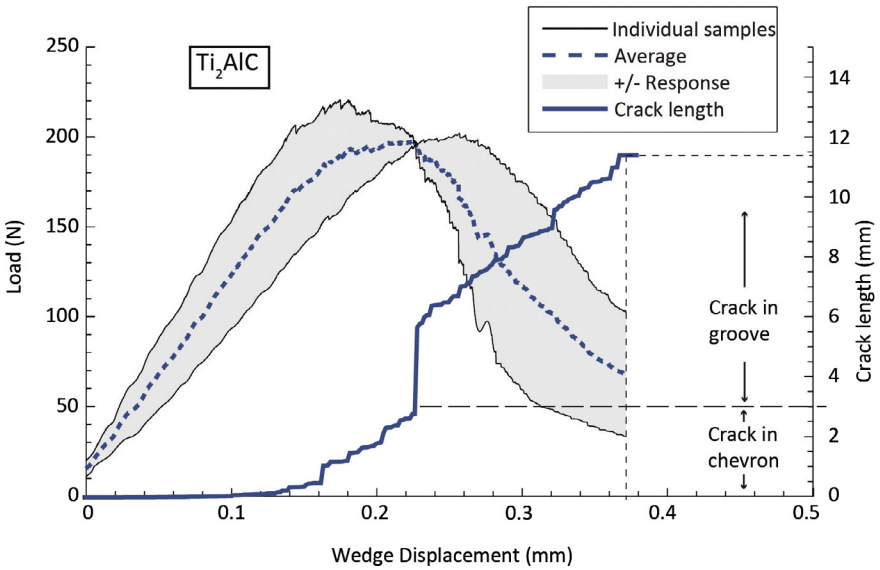

Fig. 4b. Wedge load versus wedge displacement for Ti_2AlC samples. The dashed blue line represents the average between the samples. The crack length is deduced from the acoustic energy and it is normalized using a directly measured crack length, namely 11.36 mm, at the end of the test.

The experimental results shown in Fig. 4 were conducted continuously so the acoustic energy was normalized using only the crack length at the end of the experiment, which was measured by optical and scanning electron microscopy. The final crack length recorded for the Ti_3SiC_2 sample was 9.6 mm and for Ti_2AlC sample was 11.36 mm, measured from the tip of the chevron notch.

According to the crack lengths, determined from acoustic emission data, shown in Figs. 4a and 4b, crack formation in the chevron occurred before the peak load was reached. Crack development in the chevron notch starts in the early stages of testing, at relatively low load levels. For Ti_3SiC_2 samples, as shown in Fig. 4a, the peak load appears to coincide with the instant when the crack front moves from the chevron to the uniform groove. For Ti_2AlC samples this transition apparently occurs during a fast propagation stage, so it is not possible to uniquely correlate the peak load and a specific crack length.

As shown in Fig. 4a, the load displacement curves of the individual Ti_3SiC_2 samples are relatively close to each other, reaching a peak load at approximately the same wedge displacement. The average peak load for Ti_3SiC_2 is approximately 180 N. In contrast, the Ti_2AlC samples showed more variability as observed in Fig. 4b. The peak load was reached at distinct values of the wedge displacement. Consequently, the average peak load for Ti_2AlC, which is approximately 210 N, does not exactly coincide with the peak load of the average response, which is slightly lower as shown in Fig. 4b. Nonetheless, the average response is used for comparison purposes with the simulation results as detailed in the next section.

3.2. Fracture properties

In accordance with the procedure outlined in Section 2.4, the first step is to determine the coefficient of friction between the wedge and the sample. The wedge load as a function of the wedge displacement for distinct possible values of the coefficient of friction f is shown in Fig. 5a for the Ti_3SiC_2 samples and in Fig. 5b for the Ti_2AlC samples. The simulations also include the fracture behaviour for reference purposes, although only the initial elastic response is required to determine the value of f. For the values considered, the best match for the (average) initial response is attained with a coefficient of friction $f = 0.1$ for the Ti_3SiC_2 samples and $f = 0.07$ for the Ti_2AlC samples, which are within the range of published values [34].

With the chosen coefficients of friction, simulations were conducted for distinct values of the fracture strength and the fracture energy. The wedge force as a function of the wedge displacement is shown in Figs. 6a and 6b for a fixed value of the fracture energy and various values of the fracture strength of, respectively, the Ti_3SiC_2 and Ti_2AlC samples. Similarly, Figs. 7a and 7b indicate the load-displacement response for a fixed value of the fracture strength and various values of the fracture energy.

From Figs. 6a and 6b it can be observed that, as anticipated, the fracture strength mostly affects the peak load, but the rest of the curve is somewhat similar for a fixed value of the fracture energy. In contrast, as shown in Figs. 7a and 7b, both the peak load and the energy dissipated in the process increase with increasing fracture energy for a fixed fracture strength. A comparative analysis of the results shown in Figs. 6a and 6b and 7a and 7b indicate that the peak load depends both on the fracture strength and the fracture energy. The fracture strength controls the early stage (nucleation) of cracks in the chevron while the fracture energy controls its subsequent propagation throughout the chevron and the groove. From the set of values considered in the simulations, the best fit for the average response of the Ti_3SiC_2 and Ti_2AlC samples are as follows:

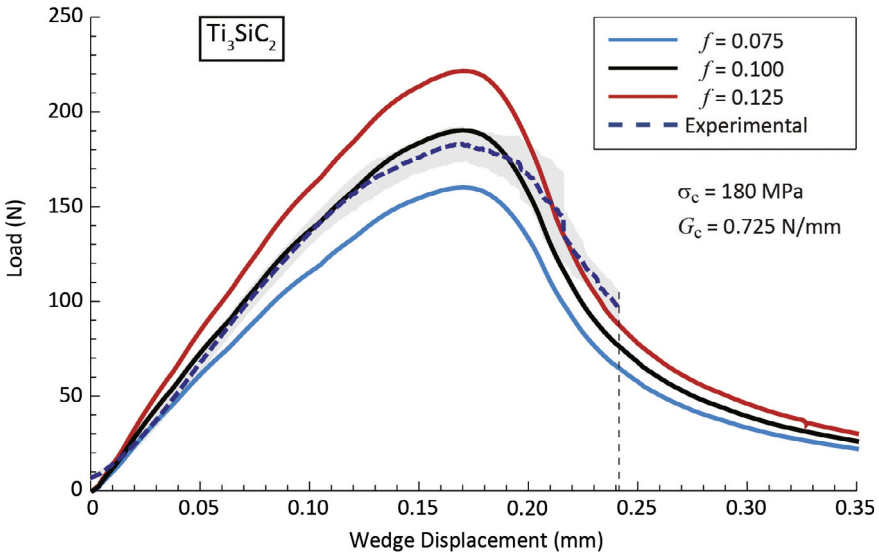

Fig. 5a. Wedge load as a function of wedge displacement for three distinct values of the coefficient of friction between the wedge and the Ti_3SiC_2 specimens. In accordance with the geometry shown in Fig. 3, higher coefficients of friction effectively provide stiffer initial responses.

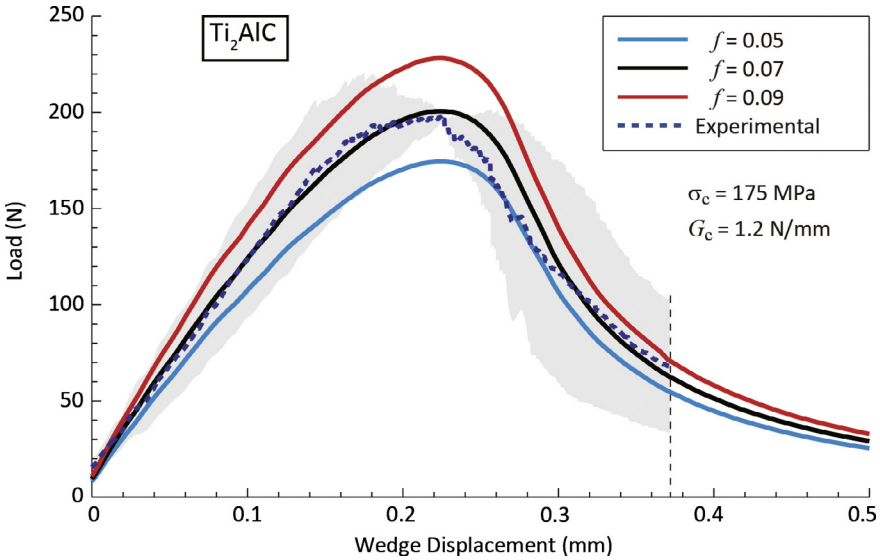

Fig. 5b. Wedge load as a function of wedge displacement for three distinct values of the coefficient of friction between the wedge and the Ti_2AlC specimens. In accordance with the geometry shown in Fig. 3, higher coefficients of friction effectively provide stiffer initial responses.

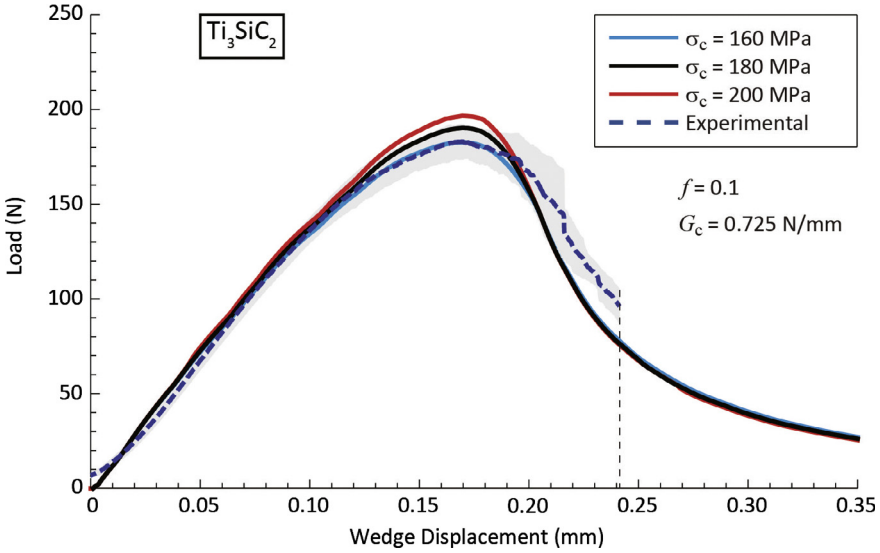

Fig. 6a. Wedge load as a function of wedge displacement for three distinct values of the fracture strength and for a fixed fracture energy of 0.725 N/mm of the Ti_3SiC_2 specimens. Within the range of values analysed (160 MPa to 200 MPa), the difference in response is mainly reflected in the peak load.

Material	Fracture strength σ_c	Fracture energy G_c
Ti_3SiC_2	180 MPa	0.725 N/mm
Ti_2AlC	175 MPa	1.2 N/mm

For Ti_3SiC_2, the predicted fracture energy value is within the range of values reported in literature [34,40,41] while for Ti_2AlC the predicted fracture energy is higher than the values reported in the literature [42,43].

To verify the capacity of the simulations to reproduce the experimental results, the predicted and measured crack length as a function of wedge displacement are shown in Figs. 8a and 8b for the same values used in the results shown in Figs. 6a and 6b (i.e., variable strength) and in Figs. 9a and 9b for the same values used in the results shown in Figs. 7a and 9b (i.e., variable fracture energy).

The simulations shown in Figs. 8a and 8b, and 9a and 9b indicate that the crack nucleates in the chevron and initially grows linearly as a function of wedge displacement. As the crack front approaches the transition region from the chevron to the groove (see Figs. 1–3), the rate of growth increases. Subsequently, the growth rate decreases as the crack front further advances into the uniform

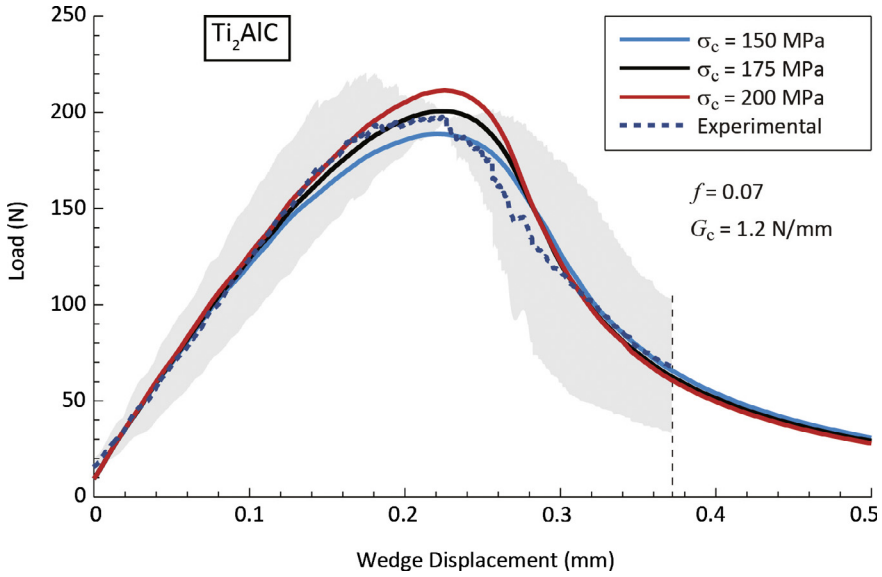

Fig. 6b. Wedge load as a function of wedge displacement for three distinct values of the fracture strength and for a fixed fracture energy of 1.2 N/mm of the Ti_2AlC specimens. Within the range of values analysed (150 MPa to 200 MPa), the difference in response is mainly reflected in the peak load.

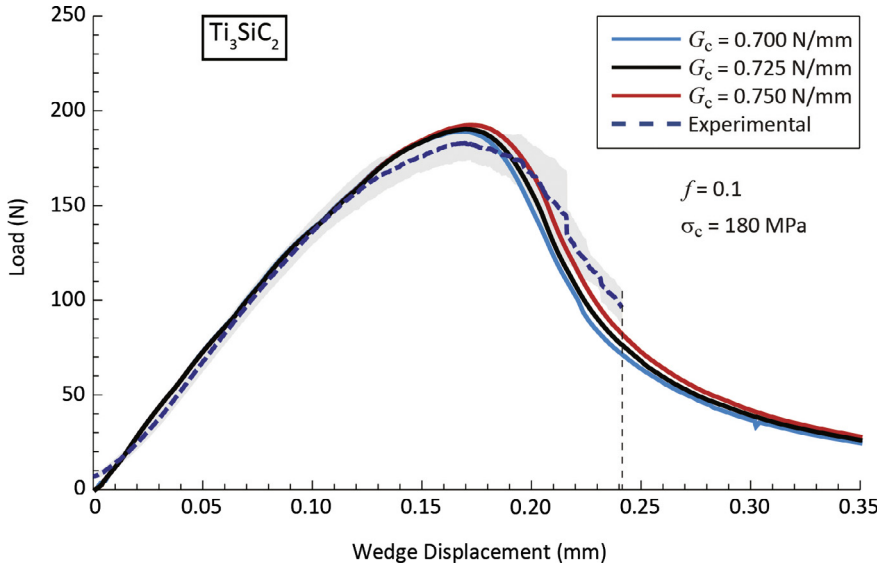

Fig. 7a. Wedge load as a function of wedge displacement for three distinct values of the fracture energy and for a fixed fracture strength of 180 MPa of the Ti_3SiC_2 specimens. As expected, the effective energy dissipated (measured as the area under the curves) increases for increasing values of the fracture energy. The best fit in terms of energy as well as the peak load is obtained with a fracture strength of 180 MPa and a fracture energy of 0.725 N/mm.

groove. For the Ti_3SiC_2 samples, as shown in Figs. 8a and 9a, it can be observed that the simulations are in good agreement with the evolution of the crack length as deduced from the acoustic signal. For the Ti_2AlC samples, as shown in Figs. 8b and 9b, the simulations initially over-predict the crack length (as deduced from the acoustic signal) but, after a sudden crack propagation, the experimental and simulated evolutions approximately coincide.

Comparing Figs. 8a and 9a for the Ti_3SiC_2 samples and Figs. 8b and 9b for the Ti_2AlC samples, it can be observed that for both materials the initial crack length is more sensitive to variations in fracture strength and, conversely, the final crack length is more sensitive to variations in fracture energy.

Using the best fit fracture parameters, it can be seen that the instant when the crack front moves from the chevron to the uniform groove corresponds to a wedge displacement of 0.2 mm for the Ti_3SiC_2 samples and 0.25 mm for the Ti_2AlC samples (see Figs. 8a and 8b). Using these values in the horizontal axis in Figs. 6a and 6b, respectively, it can be seen that the simulation predicts that the peak load occurs when the crack is still in the chevron (this effect is more pronounced for the Ti_3SiC_2 sample than for the Ti_2AlC sample).

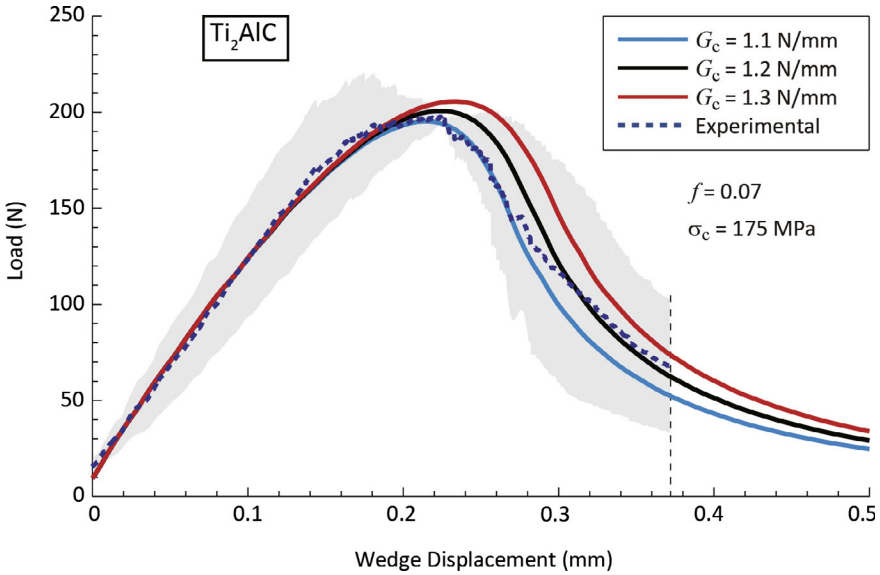

Fig. 7b. Wedge load as a function of wedge displacement for three distinct values of the fracture energy and for a fixed fracture strength of 175 MPa of the Ti_2AlC specimens. As expected, the effective energy dissipated (measured as the area under the curves) increases for increasing values of the fracture energy. The best fit in terms of energy as well as the peak load is obtained with a fracture strength of 175 MPa and a fracture energy of 1.2 N/mm.

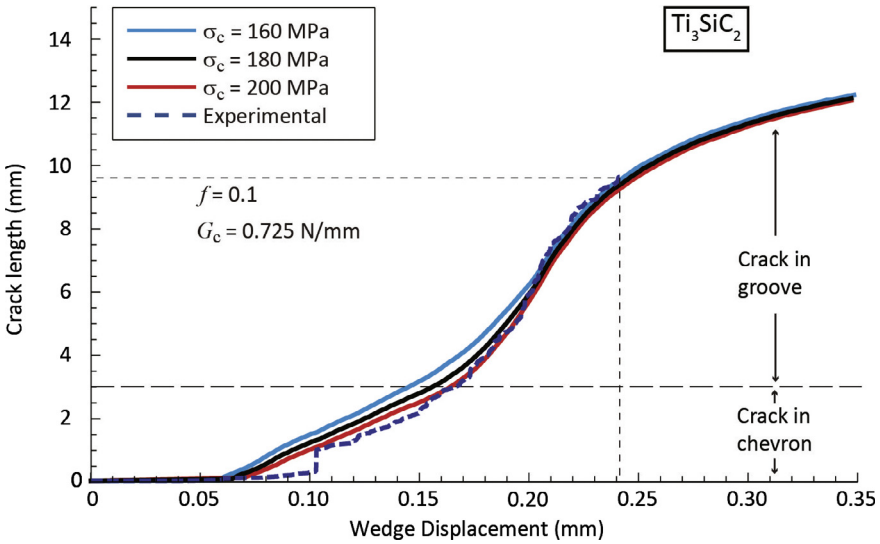

Fig. 8a. Crack length as a function of wedge displacement for three distinct values of the fracture strength and for a fixed fracture energy of 0.725 N/mm for the Ti_3SiC_2 samples.

For the range of fracture strength analysed, the simulations predict a similar total crack length at the end of the loading, which matches relatively well the experimental value. This finding suggests that crack length may be used to *estimate* the fracture properties, but it may not be sufficiently sensitive to differentiate between distinct values. Differentiation between response curves are amplified as the crack front moves from the chevron to the groove, but the inherent uncertainty of acoustic-based crack length measurement suggests that it is better to extract material properties from the load-displacement curve as indicated above.

4. Comparison of simulation-based approach with a standardized procedure: four-point bending test with chevron-notched specimen

The methodology described in the present work involves two novel aspects compared to existing (standardized) tests, namely the geometry of the specimen and the simulation-based approach to extract material properties. To cross-validate the simulation-based approach, the method was also applied to a standardized geometry for determining fracture toughness in brittle materials. To this

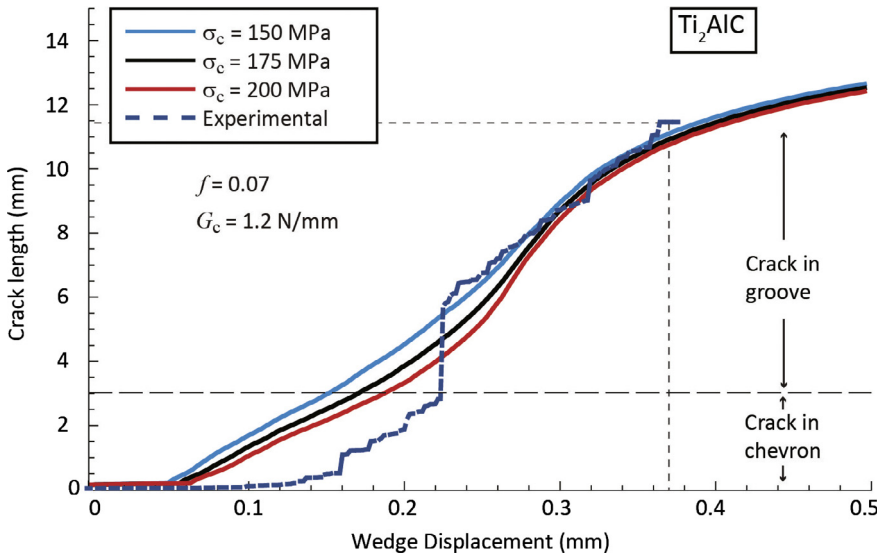

Fig. 8b. Crack length as a function of wedge displacement for three distinct values of the fracture strength and for a fixed fracture energy of 1.2 N/mm for the Ti_2AlC samples.

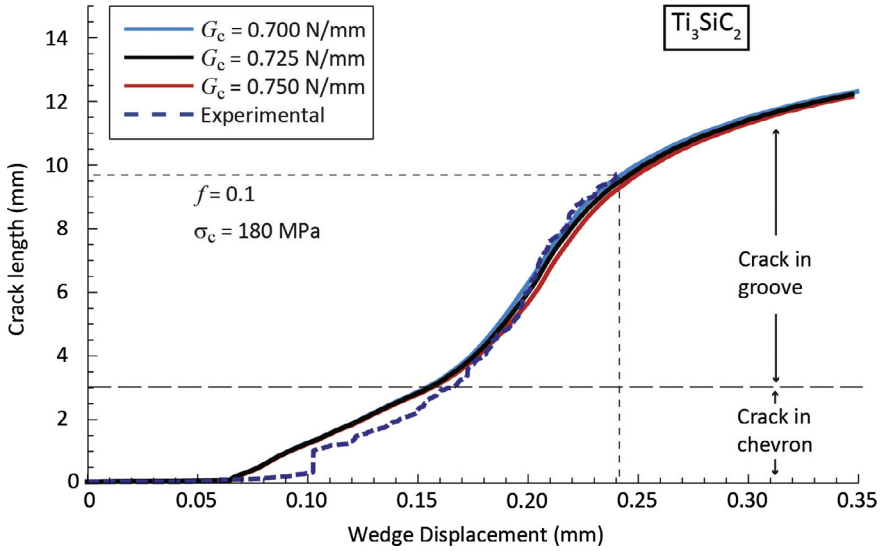

Fig. 9a. Crack length as a function of wedge displacement for three distinct values of the fracture energy and for a fixed fracture strength of 180 MPa for the Ti_3SiC_2 samples. The initial crack growth, starting around a wedge displacement of 0.07 mm in the simulations, occurs in the chevron. The crack growth rate as a function of the wedge displacement is initially approximately linear. The subsequent change in slope corresponds to the transition from the chevron to the groove, which approximately coincides with the peak load.

end, a ASTM four-point bending test with a chevron-notched specimen was used as benchmark (Standard C1421-16, see [2]). The comparison is done at the level of the post-processing of the data by comparing the simulation-based procedure and a standardized closed-form expression to extract fracture properties. Since the standardized four-point bending test is designed to extract the critical value K_{Ic} of the stress intensity factor under nominal mode I conditions, it is necessary to relate this material property to the fracture energy G_c. Assuming plane stress conditions and a small plastic zone, then the fracture energy can be related to the toughness as

$$G_c = \frac{K_{Ic}^2}{E_s} \tag{2}$$

where E_s is the Young's modulus of the specimen. For a given geometry of the chevron-notched specimen used in the four-point bending test, the ASTM standard provides a formula that uses the peak load recorded in the experiment to compute the critical stress intensity factor [2]. The ASTM model is plotted as a solid line in Fig. 10. For the numerical simulations based on the cohesive zone, the procedure is as follows: the fracture properties are given (fracture strength and fracture energy) and the test is simulated. The

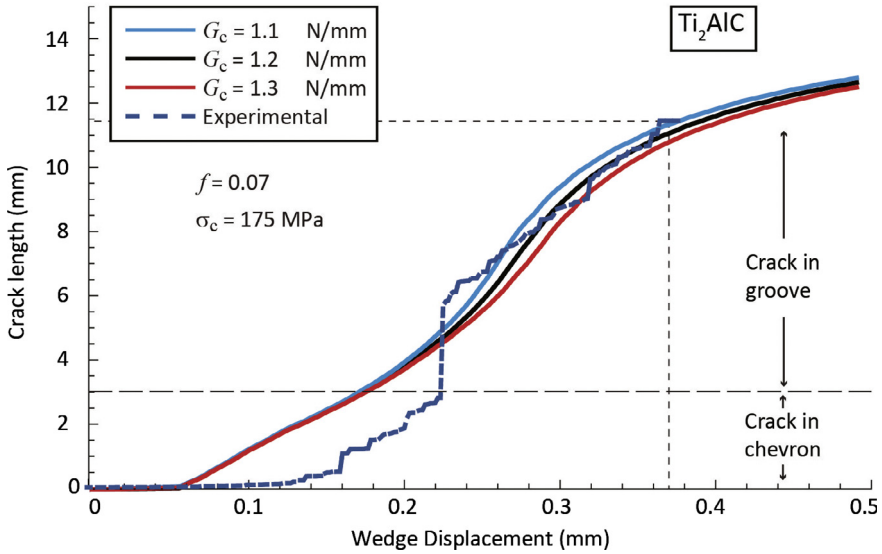

Fig. 9b. Crack length as a function of wedge displacement for three distinct values of the fracture energy and for a fixed fracture strength of 175 MPa for the Ti_2AlC samples. The initial crack growth, starting around a wedge displacement of 0.07 mm in the simulations, occurs in the chevron. The crack growth rate as a function of the wedge displacement is initially approximately linear. The subsequent change in slope corresponds to the transition from the chevron to the groove, which approximately coincides with the peak load.

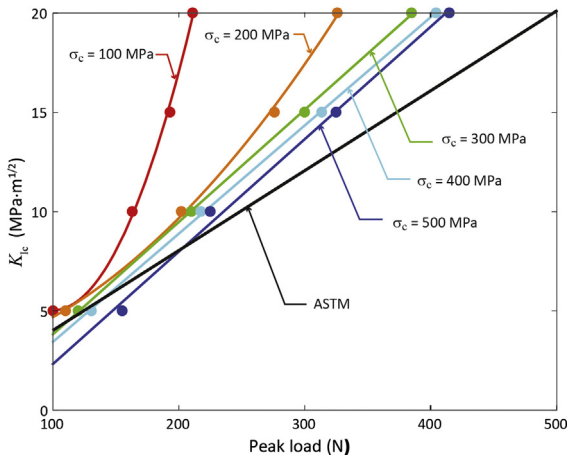

Fig. 10. Critical stress intensity factor (fracture toughness) in a chevron-notched, four-point bending specimen. The black line is obtained based on ASTM C1421-16 [2] using the peak load as independent variable. The circles represent peak loads predicted from cohesive zone-based simulations for given fracture strengths and fracture energies, from which the corresponding critical stress intensity factors are estimated assuming plane stress conditions. The corresponding lines are interpolations of the simulation points.

fracture energy is computed from the critical stress intensity factor and given elastic properties (in this case with a Young's modulus of 280 GPa) while representative values of the fracture strength are chosen. The outcome of the simulation is the peak load, which is indicated in Fig. 10 (discrete data points) for five values of the fracture strength, ranging from 100 MPa to 500 MPa. For each value of the fracture strength, a fitted curve is indicated to better visualize the predictions of the simulations. Observe that the same peak load may be obtained with distinct combinations of fracture strength and fracture energy. In contrast, the approach used to establish the ASTM formula is based on linear elastic fracture mechanics and cannot distinguish between different combinations of these two parameters. From Fig. 10 it can be observed that if the material is sufficiently brittle (i.e., relatively low fracture energy to strength ratio), the ASTM formula and the cohesive-zone simulation-based results provide comparable predictions, albeit for a limited range of fracture strengths. However, for higher values of the fracture energy, typically found in semi-brittle materials, the simulations predict a higher peak load. Note that this is only a qualitative comparison as it is not possible to ascribe a better accuracy to either procedure without access to a third reference approach deemed more precise. However, it can be concluded that for brittle materials (as intended in the ASTM analysis), the two procedures are somewhat similar while for semi-brittle and more ductile materials, the two methodologies provide different results.

The chevron-notched, four-point bending test (ASTM E399 [44]) was applied to five samples of Ti_3SiC_2 and five samples of Ti_2AlC from the same batches as the ones used in the wedge splitting test. The samples were machined from the bulk specimen by spark erosion and ground to a surface finish of 3 μm polish. However, it was not possible to achieve stable crack propagation in any sample even for relatively low loading rates. The ASTM standard considers a test to be valid only if stable crack growth can be achieved, hence these (invalid) tests are not reported in detail here. However, it is interesting to mention that the peak loads recorded would have predicted a significantly lower fracture energy compared to the values obtained from the wedge splitting test. It is also relevant to mention that the peak loads for the Ti_3SiC_2 samples were consistently lower than those of the Ti_2AlC samples, showing a similar relative ranking as the wedge splitting test (i.e., Ti_2AlC samples are tougher than the Ti_3SiC_2 samples). The most important observation, however, is that the wedge-splitting test allowed for a controlled crack growth whereas this was not possible to achieve with the four-point bending test. This demonstrates the significant benefit of the new proposed geometry for the purpose of testing healing efficiency in self-healing materials.

5. Summary and conclusions

A new chevron-notched, wedge-loaded specimen and testing method are proposed to retrieve the intrinsic fracture properties from semi-brittle materials using matching finite element calculations based on cohesive zone elements. The combination of simple test setup and advanced simulations allows unique and accurate determination of both the crack initiation and the crack propagation properties of (semi-) brittle materials while minimizing commonly necessary simplifications and assumptions. The addition of acoustic emission recording proves to be a strong tool to determine crack initiation and for tracking of crack length extension.

One important advantage of the proposed testing geometry and loading is that it allows to control crack growth and prevents full separation of the specimen. This is a critical requirement for testing self-healing materials in order to facilitate healing of the cracked surfaces. This approach was applied in Ti_2AlC samples that were cracked using a wedge-splitting test, healed and re-tested twice. Results of the self-healing testing will be presented elsewhere.

The simulations can be used to establish a simple closed-form formula for this geometry based on curve fitting. However, this would require extensive validation before it can be established as a standardized method, which is beyond the scope of the present work.

Acknowledgements

This research was sponsored in part by the European Union's seventh framework program, FP7, through the Marie Curie SHeMat ITN (grant number 290308) and the NMP SAMBA project (grant number 309849). The authors would like to thank Sathiskumar A Ponnusami for performing some simulations and for valuable discussions and feedback, as well as Hans Brouwer for his technical support and valuable experimental input.

Appendix A. Supplementary material

Supplementary data associated with this article can be found, in the online version, at http://dx.doi.org/10.1016/j.engfracmech.2018.03.014.

References

[1] Bengisu M. Engineering ceramics. Berlin Heidelberg Germany: Springer-Verlag; 2001.
[2] ASTM Standard C1421. Standard Test Methods for Determination of Fracture Toughness of Advanced Ceramics at Ambient Temperature. ASTM International, West Conshohocken, PA; 2016. http://dx.doi.org/10.1520/C1421-16, www.astm.org.
[3] Freiman SW, Mecholsky JJ. Fracture mechanics tests. The fracture of brittle materials. Hoboken, New Jersey, USA: John Wiley & Sons, Inc.; 2012. p. 32–67.
[4] Tschegg EK. Equipment and appropriate specimen shape for tests to measure fracture values. Patent AT-390328; 1986.
[5] Brühwiler E, Wittmann FH. The wedge splitting test, a new method of performing stable fracture mechanics tests. Eng Fract Mech 1990;35(1–3):117–25.
[6] Cai W, Bisschop J. Optical method for measuring slow crack growth in cementitious materials. Mater Struct 2012;45(11):1613–23.
[7] Whitlow T, Jones E, Przybyla C. In-situ damage monitoring of a SiC/SiC ceramic matrix composite using acoustic emission and digital image correlation. Compos Struct 2016;158:245–51.
[8] Sloof WG, Pei R, McDonald SA, Fife JL, Shen L, Boatemaa L, et al. Repeated crack healing in MAX-phase ceramics revealed by 4D in situ synchrotron X-ray tomographic microscopy. Sci Rep 2016;6:23040.
[9] Banks-Sills L. Update: application of the finite element method to linear elastic fracture mechanics. Appl Mech Rev 2010;63(2). 020803-020803.
[10] Nunez D, Surana KS, Romkes A, Reddy JN. J-integral for mode i linear elastic fracture mechanics in h, p, k mathematical and computational framework. Int J Comput Methods Eng Sci Mech 2009;10(5):345–69.
[11] Hillerborg A, Modéer M, Petersson PE. Analysis of crack formation and crack growth in concrete by means of fracture mechanics and finite elements. Cement Concr Res 1976;6:773–82.
[12] Schwalbe KH, Scheider I, Cornec A. Guidelines for applying cohesive models to the damage behavior of engineering materials and structures. Springer; 2013. http://dx.doi.org/10.1007/978-3-642-29494-5.
[13] Campilho RDSG, Banea MD, Chaves FJP, da Silva LFM. EXtended Finite Element Method for fracture characterization of adhesive joints in pure mode I. Comput Mater Sci 2011;50(4):1543–9.
[14] Esna Ashari S, Mohammadi S. Fracture analysis of FRP-reinforced beams by orthotropic XFEM. J Compos Mater 2011;46(11):1367–89.
[15] Qiu LP, Zhu EC, van de Kuilen JWG. Modeling crack propagation in wood by extended finite element method. Eur J Wood Wood Prod 2014;72(2):273–83.
[16] Xu Y, Yuan H. Computational analysis of mixed-mode fatigue crack growth in quasi-brittle materials using extended finite element methods. Eng Fract Mech 2009;76(2):165–81.
[17] Yang XS, Wan J, Dai CY, Zhang Y, Mao WG, Zhou YC, et al. Finite element analysis of crack propagation and fracture mechanical properties of freestanding 8 wt.

% Y_2O_3–ZrO_2 coatings. Surf Coat Technol 2013;223:87–91.
[18] Jaya BN, Jayaram V. Crack stability in edge-notched clamped beam specimens: modeling and experiments. Int J Fract 2014;188(2):213–28.
[19] Lancaster IM, Khalid HA, Kougioumtzoglou IA. Extended FEM modelling of crack propagation using the semi-circular bending test. Constr Build Mater 2013;48:270–7.
[20] Li S, Abdel-Wahab A, Demirci E, Silberschmidt VV. Fracture process in cortical bone: X-FEM analysis of microstructured models. Int J Fract 2013;184(1):43–55.
[21] Barsoum M. Physical properties of the MAX phases. In: Buschow KH, editor. Encyclopedia of materials: science and technology, 2nd ed. Oxford, UK: Elsevier; 2006. p. 1–11.
[22] Li S, Song G, Kwakernaak K, van der Zwaag S, Sloof WG. Multiple crack healing of a Ti_2AlC ceramic. J Eur Ceram Soc 2012;32(8):1813–20.
[23] Yang HJ, Pei YT, De Hosson JTM. Oxide-scale growth on Cr_2AlC ceramic and its consequence for self-healing. Scr Mater 2013;69(2):203–6.
[24] ASTM Standard E647. Standard Test Method for Measurement of Fatigue Crack Growth Rates. ASTM International, West Conshohocken, PA; 2015. http://dx.doi.org/10.1520/E0647-15, www.astm.org.
[25] ASTM Standard B962. Standard Test Methods for Density of Compacted or Sintered Powder Metallurgy (PM) Products Using Archimedes' Principle. ASTM International, West Conshohocken, PA; 2015, http://dx.doi.org/10.1520/B0962-15, www.astm.org.
[26] Ponnusami SA, Krishnasamy J, Turteltaub S, van der Zwaag S. A cohesive-zone crack healing model for self-healing materials'. Int J Solids Struct 2017;134:249–63.
[27] Ponnusami SA, Turteltaub S, van der Zwaag S. Cohesive-zone modelling of crack nucleation and propagation in particulate composites. Eng Fract Mech 2015;149:170–90.
[28] Cornec A, Scheider I, Schwalbe KH. On the practical application of the cohesive model. Eng Fract Mech 2003;70:1963–87.
[29] Li S, Thouless MD, Waas AM, Schroeder JA, Zavattieri PD. Use of a cohesive-zone model to analyse the fracture of a fiber-reinforced polymer-matrix composite. Compos Sci Technol 2005;65(3–4):537–49.
[30] Cid Alfaro MV, Suiker ASJ, De Borst R, Remmers JJC. Analysis of fracture and delamination in laminates using 3D numerical modelling. Eng Fract Mech 2009;76(6):761–80.
[31] Gruber D, et al. A laser irradiation disc test for fracture testing of refractory fine ceramics. J Eur Ceram Soc 2014;34(15):4021–9.
[32] Hille TS, Suiker ASJ, Turteltaub S. Microcrack nucleation in thermal barrier coating systems. Eng Fract Mech 2009;76(6):813–25.
[33] Turon A, Davila CG, Camanho PP, Costa J. An engineering solution for mesh size effects in the simulation of delamination using cohesive zone models. Eng Fract Mech 2007;74(10):1665–82.
[34] Gilbert CJ, Bloyer DR, Barsoum MW, El-Raghy T, Tomsia AP, Ritchie RO. Fatigue-crack growth and fracture properties of coarse and fine-grained Ti_3SiC_2. Scr Mater 2000;42(8):761–7.
[35] Barsoum MW, Radovic M. Elastic and mechanical properties of the MAX phases. Annu Rev Mater Res 2011;41:195–227.
[36] Gan YP, Qian XK, He XD, Chen YX, Yun SN, Zhou Y. Structural, elastic and electronic properties of a new ternary-layered Ti_2SiN. Phys B-Condens Matter 2011;406(20):3847–50.
[37] Bassim MN, St. Lawrence S, Liu CD. Detection of the onset of fatigue crack growth in rail steels using acoustic emission. Eng Fract Mech 1994;47(2):207–14.
[38] Moorthy V, Jayakumar T, Raj B. Acoustic emission behaviour during stage II fatigue crack growth in an AISI type 316 austenitic stainless steel. Bull Mater Sci 1994;17(6):699–715.
[39] Roberts TM, Talebzadeh M. Acoustic emission monitoring of fatigue crack propagation. J Constr Steel Res 2003;59:695–712.
[40] Radovic M, Barsoum MW, El-Raghy T, Wiederhorn SM, Luecke WE. Effect of temperature, strain rate and grain size on the mechanical response of Ti3SiC2 in tension. Acta Mater 2002;50(6):1297–306.
[41] El-Raghy T, Barsoum MW, Zavaliangos A, Kalidindi SR. Processing and mechanical properties of Ti_3SiC_2. II. Effect of grain size and deformation temperature. J Am Ceram Soc 1999;82(10):2855–60.
[42] Barsoum MW, Ali M, El-Raghy T. Processing and characterization of Ti_2AlC, Ti_2AlN and $Ti_2AlC_{0.5}N_{0.5}$. Metall Mater Trans A 2000;31(7):1857–65.
[43] Wang XH, Zhou YC. Solid-liquid reaction synthesis and simultaneous densification of polycrystalline Ti_2AlC. Zeitschrift fur Metallkunde 2002;93(1):66–71.
[44] ASTM Standard E399. Standard Test Method for Linear-Elastic Plane-Strain Fracture Toughness KIc of Metallic Materials. ASTM International, West Conshohocken, PA; 2013. doi: 10.1520/E0399-12E03, www.astm.org.